Investigation of Sediment-Rich Glacial Meltwater Plumes Using a High-Resolution Multispectral Sensor Mounted on an Unmanned Aerial Vehicle

Kornelia Anna Wójcik, Robert Józef Bialik *, Maria Osińska and Marek Figielski

Institute of Biochemistry and Biophysics, Polish Academy of Sciences, Pawińskiego 5a, 02-106 Warsaw, Poland; kwojcik@ibb.waw.pl (K.A.W.); maria.osinska@ibb.waw.pl (M.O.); marek@vanilla.pl (M.F.)

* Correspondence: rbialik@ibb.waw.pl

Abstract: A Parrot Sequoia+ multispectral camera on a Parrot Bluegrass drone registered in four spectral bands (green, red, red edge (RE), and near-infrared (NIR)) to identify glacial outflow zones and determined the meltwater turbidity values in waters in front of the following Antarctic glaciers: Ecology, Dera Icefall, Zalewski, and Krak on King George Island, Southern Shetlands was used. This process was supported by a Red-Green-Blue (RGB) colour model from a Zenmuse X5 camera on an Inspire 2 quadcopter drone. Additional surface water turbidity measurements were carried out using a Yellow Springs Instruments (YSI) sonde EXO2. From this research, it was apparent that for mapping low-turbidity and medium-turbidity waters (<70 formazinenephelometricunits (FNU)), a red spectral band should be used, since it is insensitive to possible surface ice phenomena and registers the presence of both red and white sediments. High-turbidity plumes with elevated FNU values should be identified through the NIR band. Strong correlation coefficients between the reflectance at particular bands and FNU readings ($R_{Green} = 0.85$, $R_{Red} = 0.85$, $R_{Edge} = 0.84$, and $R_{NIR} = 0.83$) are shown that multispectral mapping using Unmanned Aerial Vehicles (UAVs) can be successfully usedeven in the unfavourable weather conditions and harsh climate of Antarctica. Lastly, the movement of water masses in Admiralty Bay is briefly discussed and supported by the results from EXO2 measurements.

Keywords: water reflectance; turbidity; unmanned aerial vehicle; glacier

1. Introduction

The Antarctic and Southern Ocean influence the climate of the entire world. For instance, the sea level of the oceans is dependent on Antarctic ice sheet shifts caused by climate change [1,2]. The West Antarctic Peninsula is especially vulnerable to the impact of rising temperatures, as it is one of the most rapidly warming regions in the world [3,4]. However, it should be noted that a cooling effect was recently observed in this region [5,6]. Marine-terminating glaciers are unique areas of the Antarctic Peninsula region sensitive to changes in the basal water supply as well as sensitive to the thinning of the terminus, with faster flow leading directly to the sea level rise [7]. According to Vaughan [8], the velocity of glacier melting in this area doubled from 1950 to 2000, and provided increased meltwater and sediment influx, which changes the functional attributes of marine ecosystems [4].

Sediment discharge in glacier meltwater is caused by two distinct mechanisms [9,10]. The first mechanism is triggered by subglacial water pressure creating cracks in bedrock that allow residue transport through upper ice levels, and the second mechanism is caused by the abrasion of bedrock by the rocks suspended in the basal ice layer. This sediment is transported with meltwater as subglacial discharge to the inlet or fjords [11–17] (Figure 1). If enough sediment and meltwater is provided, suspended matter will surface and form high-turbidity plumes on the water surface [18] (Video S1).

Figure 1. Photograph of a meltwater conduit at the margin of Zalewski Glacier.

A large glacial sediment discharge has an impact on the salinity and temperature of seawater [4], biodiversity, the productivity as well aswell-being of marine flora and fauna, and, dependent on the latter, land animals and birds [19–25]. Consequently, changes in polar ecosystems require monitoring. However, due to thelimitations created by harsh climates and terrain inaccessibility, there has been a recent shift from an emphasis on field work measurements to remote sensing analysis [10,13,18,26–28]. In contrast to West Greenland in the Arctic, where river-fed plume monitoring is relatively common [28–31], these kinds of observations in Antarctica remain scarce, while limitingthe identification of plumes and their influences on ecosystems. Moreover, Hodgkins [29] claimed that "Plume monitoring, therefore, requires validation in a range of environments and in different seasons."

Satellite observation of water turbidity has become an indicator fordetermining the water quality but is also a proxy for the suspended-sediment concentration (SSC) [32]. Observations of ocean water optical properties, specifically variations in turbidity, using remote sensing methods, have been intensively conducted worldwide [32–35]. However, the use of similar methods in coastal monitoring research in the polar regions is still relatively limited [36]. The main reasons for such limitations are extensive cloud coverage in polar marine region monitoring and the occurrence of polar day and polar night, which reduces the chances of satellite monitoring. Fortunately, unmanned aerial vehicle (UAV) technological advancements now allowobservations of spatial and temporal processes and phenomena that were previously unachievable through conventional remote sensing methods [37]. The main advantages of using UAV are the high pixel resolution and the possibility of choosing the place and time of the flight, adapted to the needs of the research.

Consequently, the objective of this study is to assess the possibility of using a multispectral sensor, such as Parrot Sequoia+, supported by a Zenmuse X5 camera for (1) identifying glacial outflows and (2) estimating turbidity values of the sediment plumes based on UAV observations. These plumes areidentified by turbidity concentrations. To achieve these goals, during the 2019 austral summer in the Admiralty Bay in West Antarctica, recurrent plumes in front of four glaciers, which differ in shape, dynamics, and geological location, were investigated, and their plume waters were examined.

2. Materials and Methods

2.1. Study Area

Water turbidity, as a relative measure [38], is impacted by the physical attributes of suspended sediment (e.g., the size, shape, and colour of particles), which are determined mainly by its geological origin [39,40]. Admiralty Bay is situated on three tectonic blocks separated by the Ezcurra and Mackellar Faults (Figure 2). These faults are composed of various minerals and are located on coasts mainly covered by glacial ice [41,42]. The sediment type transported by the glacial meltwater comes from bedrock. Therefore, due to its tectonic diversity, Admiralty Bay provides a unique opportunity to assess turbid plumes created by freshwater filled with heterogeneous sediment (Figure 2, Table 1).
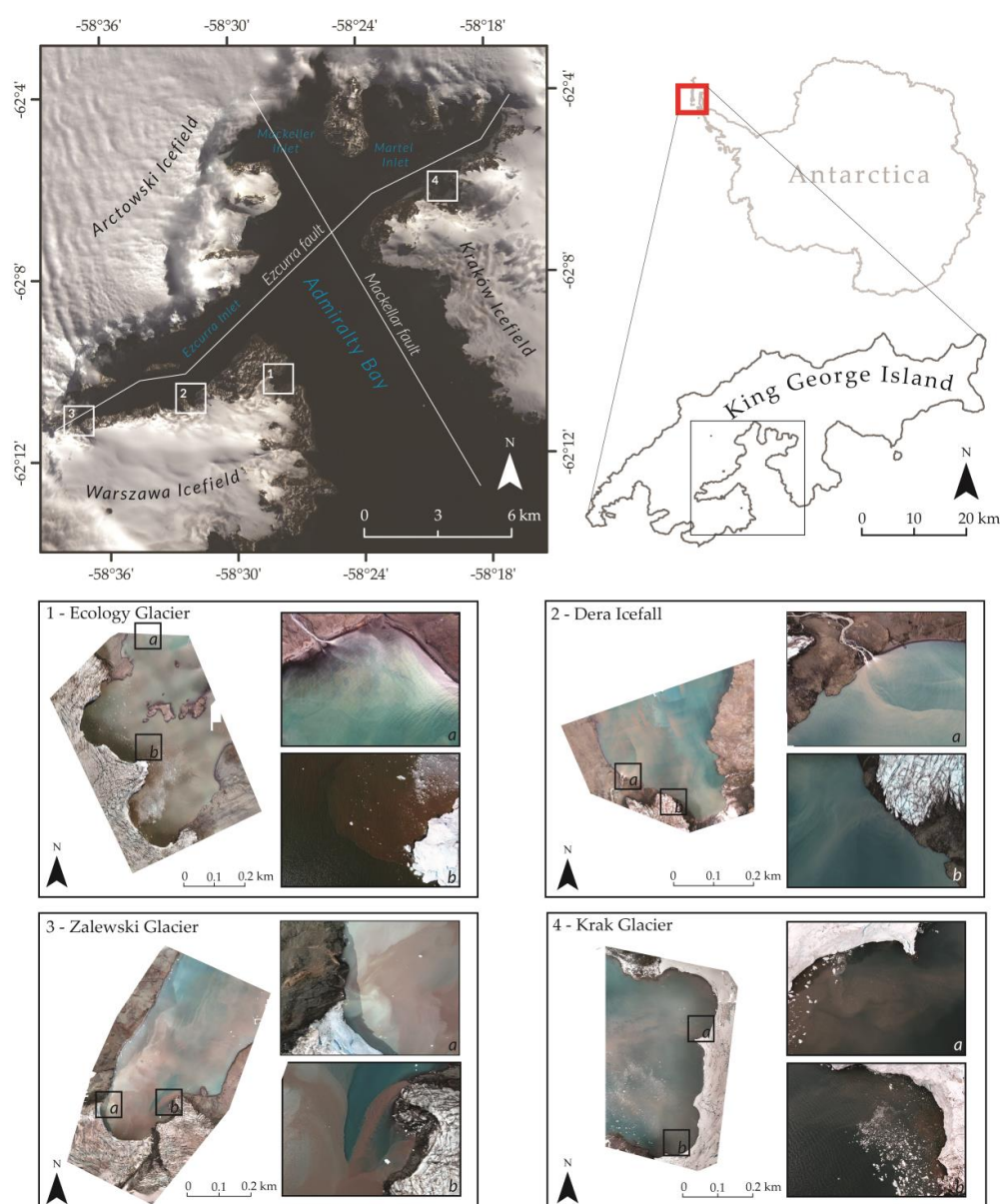

Figure 2. Satellite images (Landsat 8, acquired on 10 March 2018) showing the locations of the selected glaciers (white frames): 1—Ecology Glacier, 2—Dera Icefall, 3—Zalewski Glacier, 4—Krak Glacier. Black frames labelled a and b mark the positions of subglacial discharges and surface runoffs to particular glacier-front coves (images produced by a Zenmuse X5 camera from the Inspire 2 quadcopter drone).

To analyse the widest possible range of turbid waters, depending on sediment characteristics, four glacier fronts were chosen as a research area: Zalewski Glacier (situated directly over the Ezcurra Fault, drawing from two different tectonic formations), Dera Icefall, Ecology Glacier, and Krak Glacier (characterized in Table 1, Figure 2). All four fronts are based on specific bedrocks and are adjoined by coves (in accordance with Commission on the Standardization of Geographical Names (KSNG) guidelines [43]), which shelter turbulent waters from rapid mixing that would disrupt plume arrangements.

It should be noted that tides are the factor that markedly impose a certain rhythm on other processes occurring in Ezcurra Inlet, as already suggested by Dera [44]. They are irregular with 12-h intervals, and the amplitude of sea level variations attain its maximum values in two-week cycles with the diurnal variation of sea level occasionally exceeding even 2 m [44]. Moreover, Pruszak [45] claimed that tides are the decisive factor causing a determined water circulation in Admiralty Bay when the wind speed is below 3 ms^{-1}. Such weather conditions, with low wind speed, are usually expected to collect the data using drones. Additionally, in the case of tides, independently from their phase, the inflow along the eastern and western coasts of Admiralty Bay is usually observed [46]. It could have affected the sediment flux in front of the Ecology Glacier, which is located on the western shore of Admiralty Bay. Tides heights during the day of measurements are presented in Table 2.

Table 1. Geological and morphological characteristics of the selected glaciers.

Selected Glacier	Tectonic Formations (Birkenmajer [41])	Geological Bedrock (Birkenmajer [41])	Active Front Altitude (m)	Active Front Width (m)/Length of Front Adjoining Cove Waters (m)	Cove Name, Area (km²)	Sun Exposure	Glacial Retreat Ratio 1956–1995 (Braun and Gossman [47]) (%)
Ecology Glacier	Llano Point Formation (Warszawa Block)	Basalts and andesites alternating with agglomerates and tuffs	~40	1185/880	Suszczewski Cove/0.359	NE	5.9
Dera Icefall	Point Thomas Formation (Warszawa Block)	High-aluminium basalts, breccias	-	Retreated from the waterfront	Hervé Cove/0.182	N	3
Zalewski Glacier	Two formations divided by the Ezcurra Fault: Znosko Glacier Formation (Barton Horst)/ Point Thomas Formation (Warszawa Block)	Andesites, tuffs, and agglomerates/ high-aluminium basalts, breccias	~33	445/255	Unnamed Cove/0.180	NE	0.9, but since 1995, it has rapidly retreated further
Krak Glacier	Mount Wawel Formation (Warszawa Block)	Terrestrial volcanics with plant-bearing strata	max 46	785/785	Lussich Cove/0.181	NW/W	20.9

2.2. Field Measurements

In previous research, two methods of plume identification were mainly described: through water turbidity measurements (optical measurement methods) [32,34] and with water filtration and assessing the suspended-sediment concentration (SSC) [48]. During the austral summer of 2019, 70 water samples from six fjords were taken in 1-L bottles. First, the turbidity of the water samples was optically measured in formazinenephelometricunits (FNU) by a Yellow Springs Instruments (YSI) sonde EXO2 using an optical sensor to measure the SSC (including silt, clay, sand, algae, and organic matter). In accordance with YSI guidelines [48], a two-point calibration of the sensor was conducted using 0 (deionized water) and 12.4 FNU standards for low-turbidity waters. The sensor used has an accuracy

of 2%. Afterward, the samples were filtered, and the filters were dried and weighed, which allowed for an SSC calculation.

The correlation between the measured water turbidity in FNU and the SSC in mg/L was 0.96 (Figure 3), which confirms that the optical turbidity measurement method for the identification of subglacial water discharges is appropriate. In contrast to the collection of water samples to investigate the SSC, the main advantages of turbidity measurements are the possibility of rapid collection of a very large amount of data and the production of high-frequency measurements that allow the observation of continuous changes in the dynamic environment of sediment plumes. Thus, in this paper, we focus on the optical turbidity instead of the SSC. In addition, the measurements of turbidity were run on a surface layer of water (a depth of 20–30 cm) with a 1-s interval and were conducted from the deck of a Zodiac Nautic inflatable boat.
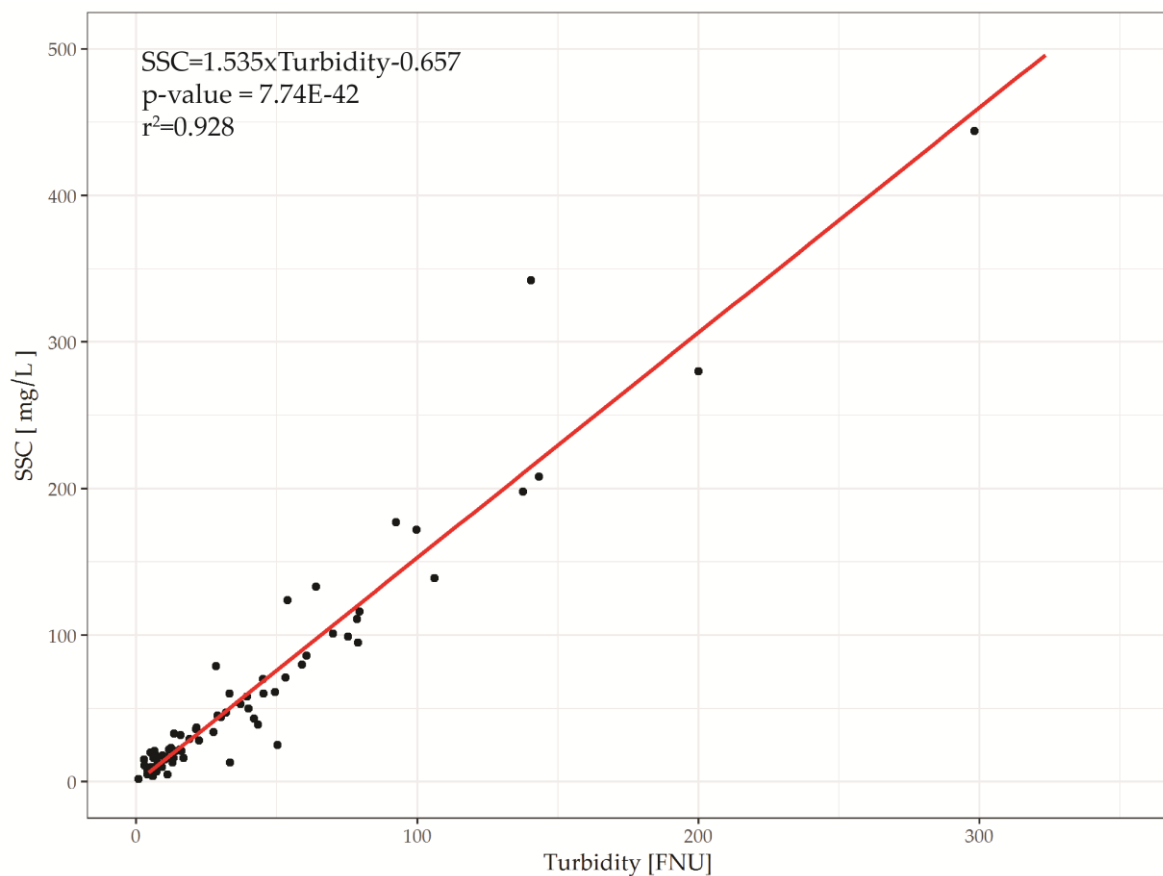

Inside the plot:
$$SSC = 1.535 \times Turbidity - 0.657$$
p-value = 7.74E-42
$$r^2 = 0.928$$

Figure 3. Scatter plot of the relationship between the suspended-sediment concentration (SSC) (mg/L) and the turbidity (formazinnephelometricunits, FNU).

Figure 4 shows the vertical distributions of water temperature, turbidity, and salinity in front of the Zalewski Glacier on 15 February, 2019. All parameters show significant variation in the surface layer, which has a depth of about 1.5–3.0 m. Similar results were obtained by Dera [44]. This demonstrates the impact of meltwater from the glacier and indicates the boundary layer between salt and fresh water.
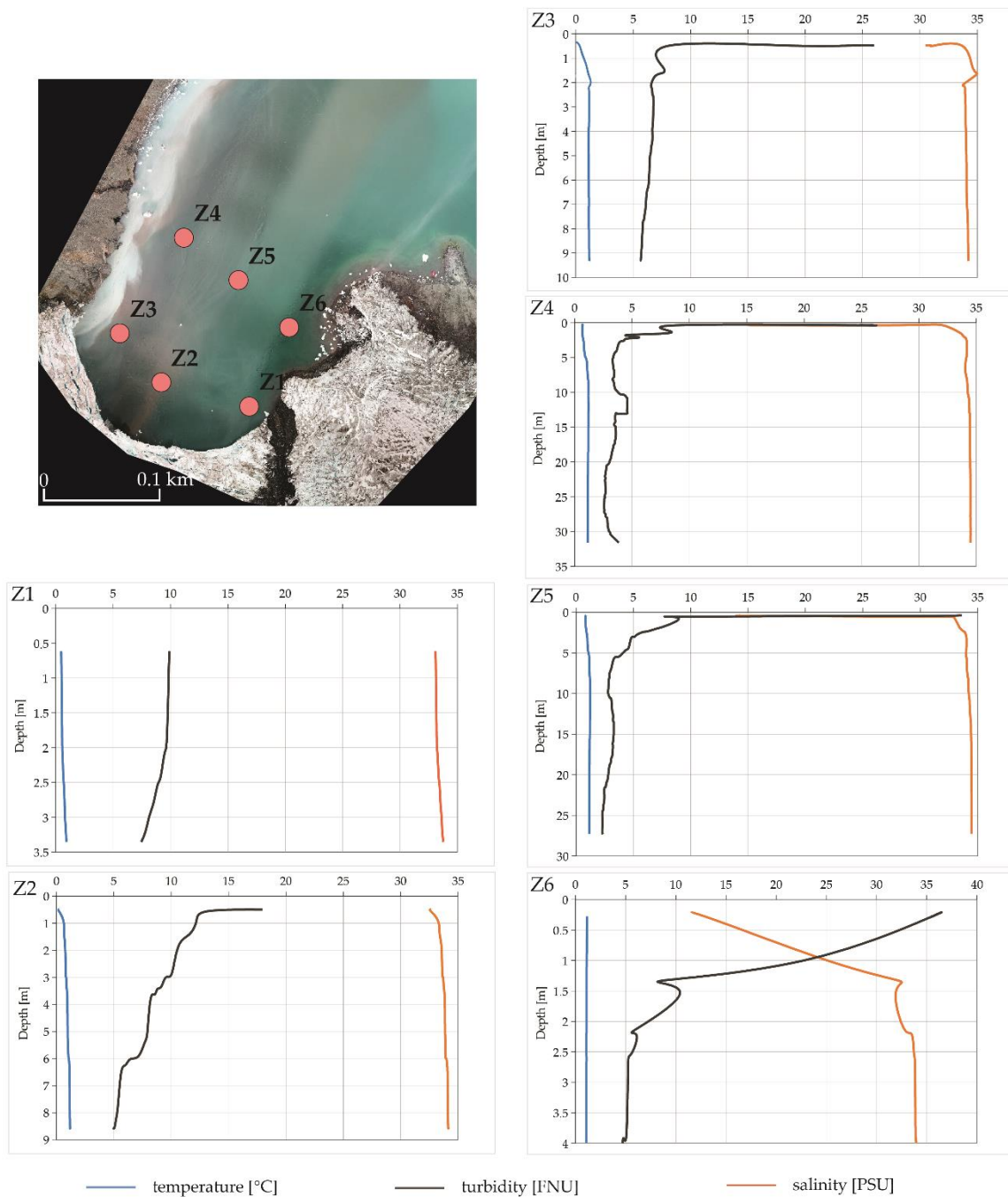
Figure 4. Vertical distributions of water temperature, turbidity, and salinity in front of the Zalewski Glacier on 15 February 2019.

2.3. UAV Data Acquisition

The Parrot Sequoia+ instrument is a set of two integrated sensors. The multispectral sensor, directed downward, is a combination of four narrow band cameras that measure the reflected solar radiation in the green (530–570 nm), red (640–680 nm), red edge (RE) (730–740 nm), and near-infrared (NIR) (770–810 nm) wavelengths. The second sensor, directed upward, measures the amount of incoming solar radiation in the same wavelength range as reflected solar radiation, which allows radiometric self-calibrations of the camera. Moreover, attached calibration targets increase the radiometric accuracy of the photographs and enable comparisons of the data acquired from separate UAV flights with non-identical light conditions. The Parrot Sequoia+ sensor was assisted by a Zenmuse X5 camera,

with a Micro Four-Thirds (MFT) and a 15-mm focal length, 72° field of view (FOV), a 4K resolution while filming at 30 frames per second (FPS), and 16-megapixel images. The Zenmuse X5 camera with a standardized Red-Green-Blue colour model (sRGB) was used to identify subglacial discharges and to validate the spectral images.

The Parrot Bluegrass drone flyover was undertaken first, which was immediately followed by the Inspire 2 mission and, subsequently, the turbidity measurements took place *in situ*. The Parrot Sequoia+ multispectral sensor was mounted to a UAV quadcopter (Parrot Bluegrass) that flew over four test fields (Figure 2). The drone carries out precise, 2-km missions using the Parrot Sky controller gear and an independent flight planning system. The device is 802.11ac Wi-Fi-enabled, which allows the recording of the front camera transmission onto the controlling panel. The Zenmuse X5 camera was installed onto the Inspire 2 quadcopter drone, with a maximum flight speed of 36 km/h and an autonomous heating system that allows functioning at low temperatures (down to −20 °C). Forward-facing and downward-facing vision systems create an intelligent obstacle avoidance system that is especially useful in mountainous terrain.

During the measurement phase (Table 2), the Parrot Bluegrass overflight was carried out. Immediately afterward, the same drone mission was repeated by Inspire 2. To prevent boat trails from interfering with the registered imagery, *in situ* turbidity measurements with the sonde were performed following the flyovers.

Flights took place during rapidly changing cloud cover. The mean daily wind speed during mission days oscillated between 2 and 5 ms^{-1}, and rapid shifts in cloud cover occurred. These changes were addressed through additional radiometric calibrations, based on the calibration targets (a white balance card giving the reflectance properties of the card across the spectrum of light captured by the camera), before every Parrot Bluegrass flight. The use of a radiometric calibration target enables the software to calibrate and correct the image's reflectance from separate UAV flights with non-identical conditions. Missions were planned with Pix4DCapture. For each mission, flight specifications (e.g., the flight altitude and number of photographs) varied due to topographic factors, including differing cove surfaces as well as uneven heights of the orographic obstacles (Table 2, Figure 5).
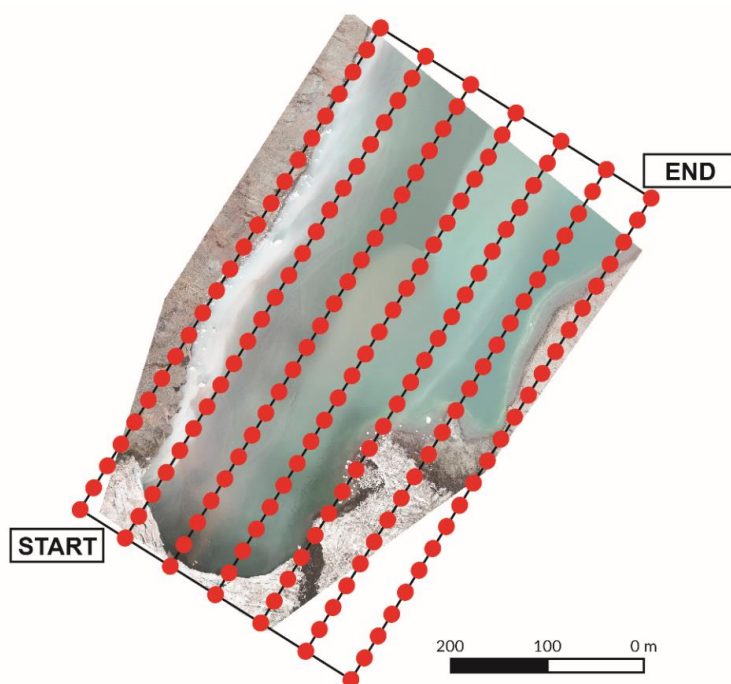

Figure 5. Flight plan example showing image waypoints and flight lines on the Zalewski Glacier.

Table 2. Flight specifications (Parrot Sequoia+).

Glacier	Area Covered by the UAV Mission	Number of Photographs Taken during the Mission	Flight Altitude	Ground Sampling Distance (GSD)—Pixel Resolution	Mission Date	Tide Height during Measurements
Ecology	0.23 km²	980	110 m	11.7 cm	26 January 2019	1.41 m to 1.19 m
Krak	0.32 km²	1440	145 m	15.2 cm	31January 2019	0.49 m to 0.58 m
Zalewski	0.33 km²	740	150 m	15.4 cm	28 January 2019	1.09 m to 0.99 m
	0.32 km²	616	150 m	15.2 cm	10 February 2019	1.15 m to 1.08 m
Dera	0.22 km²	448	155 m	14.02 cm	9 February 2019	0.60 m to 0.67 m

2.4. Image Postprocessing

Image postprocessing was performed using Pix4Dmapper Pro. Using Parrot Sequoia+ photographs and AgMultispectral template remote sensing reflectance (Rrs). Maps were created for each band. Radiometric correction was executed using radiometric corrections of the camera and light sensor (i.e., the internal correction of the camera and light sensor) and values given by the calibration target. Due to the homogeneity of the water surface and the artefacts created during the orthomosaic preparation, noise filtering was conducted, which filtered out incorrect points in the point cloud and corrected their altitudes based on neighbouring data. Cases in which the surfaces were inaccurately convex were corrected with surface smoothing. Statistical descriptions of the flyovers foreach glacier are provided in Table 3. For missions with less than 1000 keypoints (distinctive values for homogenous areas), the root mean square error (RMSE) was 2–3 m without additional ground control points (GCPs), whereas the mean re-projection error was less than one pixel, which is acceptable in this type of analysis.

Table 3. Quality report of the completed mission.

Glacier	Root Mean Square Error (m)		Mean Re-Projection Error (pixels)	Key Points Image Scale
	X	Y		
Ecology	2.15	2.20	0.525	9797
Krak	3.21	3.71	0.436	8979
Zalewski 1	3.09	2.92	0.325	9067
Zalewski 2	2.42	2.14	0.386	8990
Dera	2.85	1.90	0.326	9250

Zenmuse X5 photographs were used as the basis for orthophotomaps of the respective test fields. By using images in a natural colour model, it was possible to outline the shapes of the surface plumes, and through the percent clip histogram method [49], which sharpens particular colour tones, it was possible to identify the prevalent sediment colour. To retrieve the predominant sediment colour, the maximum RGB algorithm [50] was applied. To match the maximal/minimal intensity of the channel for every pixel, RGB values were used. Initially, the maximum of the R, G, and B values (m = max(r,g,b)) was determined. If R < m, then R = 0. If G < m, then G = 0. If B < m, then B = 0. This algorithm allows us to indicate the most contributing channel in a given area of an image. As a result, it was possible to separate homogenous sediment types and determine the shapes of the plumes. In all five analysed cases, two types of sediments (Figure 6) were distinguished. Sediment A was observed within each cove and contains one predominant channel: red. Sediment B was seen near only the Zalewski Glacier and, unlike the previous type, it includes two components: mostly green and less blue.
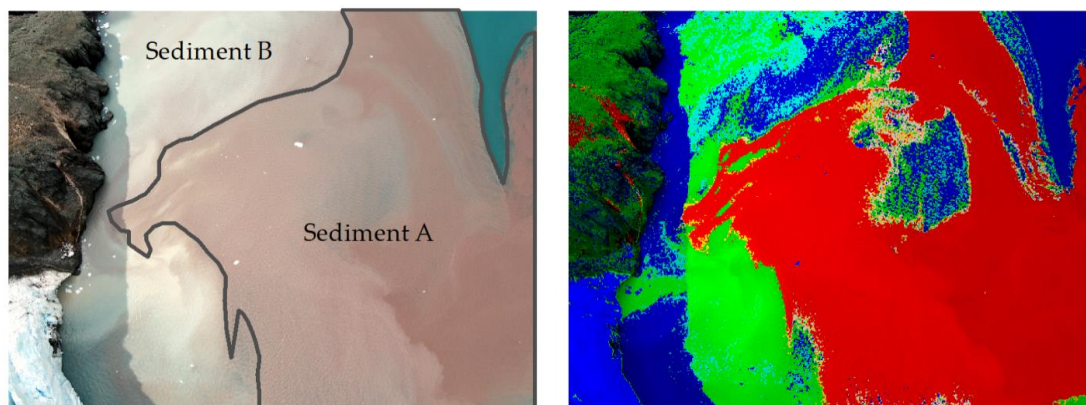
Figure 6. An example of an application of the maximum RGB algorithm.

2.5. Data Analysis

Each band's reflectance map was linkedwith the surface turbidity measurements using ArcMap 10.6 (Esri, Redlands, CA, United States). The goal was to prepare the data for a statistical analysis that would compare values of individual pixels' reflectance with the singular turbidity reading *in situ*. Initially, the EXO2 data were cleaned by removing the result-disturbing mismeasurements and artefacts that resulted from instrument utilization and boat movement interference. To avoid redundancy, the data were reduced, leaving every third turbidity value. Afterward, using the spatial optimization method [51], a 1-m-radius buffer area was designated around each measurement point to reduce, to the fullest possible extent, the water fluidity and mirroring effects as well as single pixels' artefacts. Then, using MATLAB, every *in situ* measurement was assigned a mean reflectance value of the buffer area, and thecorrelation between the turbidity and the remote sensing reflectance was calculated.

3. Results

As apparent from the maps in Figure 7, the water turbidity values, as well as the spectral reflectance registered by the Parrot Sequoia+ cameras, differ significantly between specific coves. Furthermore, the reflectance range, visibility, and plume shapes are notably dependent on the registered electromagnetic wavelength. In all five analysed cases, the highest reflectivity was recorded in the green electromagnetic spectrum. The reflectance in this band was larger than 10%, with water turbidity values <10 FNU. A disproportionately high reflectance was noted at a distance of 500 m from the glacier terminus, and, in some cases, it covered 80% of the cove's water surface (Figure 7b,d).

Reflectance in the red spectral band is most effective for lower turbidity (<70 FNU) and is less susceptible to values greater than 140 FNU. Nonetheless, the shapes of the plumes visible in this band most closely imitate the outflows depicted by the Zenmuse X5 camera (Figure 7c). In the RE and NIR spectral regions, high-turbidity waters are most effectively visualized with a value larger than 60 FNU, but these ranges are not responsive to low-turbidity waters. Increased turbidity, which was caused by water discharge at the glacier front [52], is visible in the red spectral band (Figure 7b). In occurrences of high-turbidity water outflows, the distinction can also be made with longer wavelengths rather than visible spectral bands (Figure 7d).

Due to contrasting spectral reflectance maps with orthophotomaps in the natural RGB colour model registered through the Zenmuse X5 camera, it was possible to identify subglacial discharges with a natural sediment colour, depending on the geology of the bedrock. In the area with four coves, two types of sediment were detected: predominantly sediment A with red pigmentation and, to a lesser extent, sediment B with white pigmentation. In the green spectral band, sediment B reflects more intensely than sediment A (Figure 7c). The reflectance ranges of the red spectral band for sediment A and sediment B are proportionate. Yet the NIR and RE spectral region rates are more driven by sediment B (Figure 7c).

The occurrence of glacier ice (i.e., mélange, growlers, and ice packs) on the cove water surfaces is frequent (Figure 7a,e). The green spectral band is the most susceptible to ice (Ecology Glacier and Krak Glacier), which has a disproportionately high reflectivity. Contradictory results are found in the NIR spectral band, where ice is characterized by only a high reflectance, and fine surface plumes are indistinguishable. High reflectance values in the red spectral band lead to the identification of ice. Moreover, in this spectral region, ice does not interfere with the identification of subglacial discharges (i.e., there is no increase in the reflectance coefficient values as in the green spectral band, nor is there a decrease, as in the NIR spectral band).

The combination of red+NIR bands and the relation between red/NIR was also examined. The sum of the reflectance of these channels provides a sharpened image of high-turbidity waters (>70 FNU) (Figure 7c) and information on the occurrences of ice packs and growlers (Figure 7a). Using this combination method, the presence of a mélange phenomenon may lead to an incorrect analysis because of its negative impact on plume creation (Figure 7e). The image obtained by calculating the red/NIR relation presents a contrast between high-turbidity waters (>70 FNU) and lower turbidity waters. Red sediment discharge (sediment A) is more visible than white sediment discharge (sediment B) (Figure 7c). Additionally, ice occurrences become unidentifiable using this formula (Figure 7e). However, overlapping both the red+NIR and red/NIR images helps indicate areas with increased glacial sediment, which, simultaneously, allows for the identification of ice packs, growlers, and mélange.
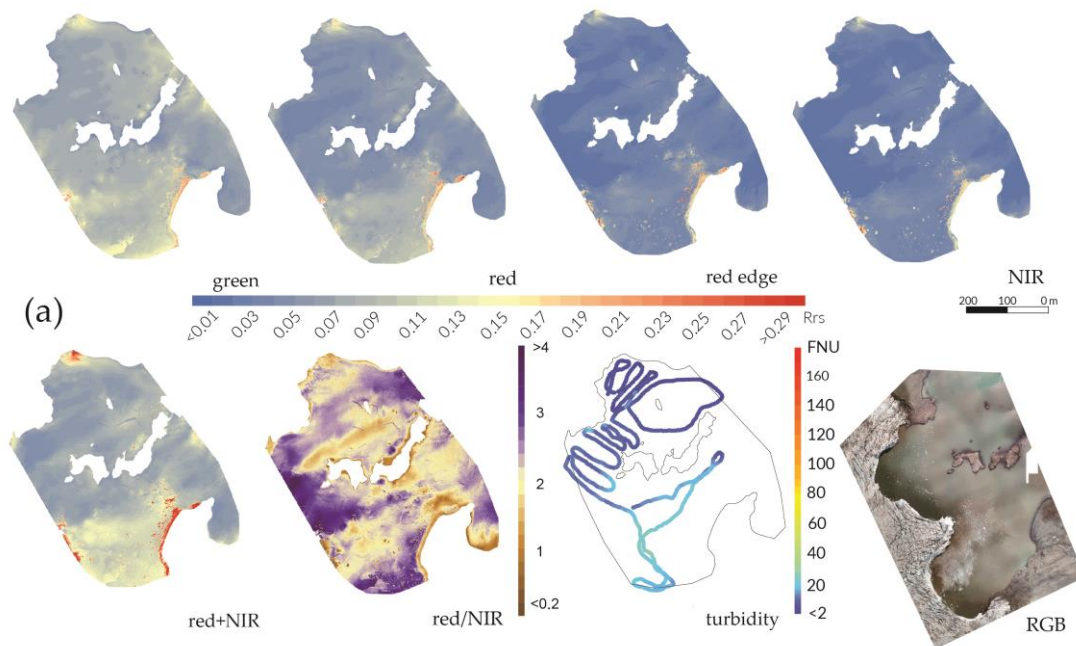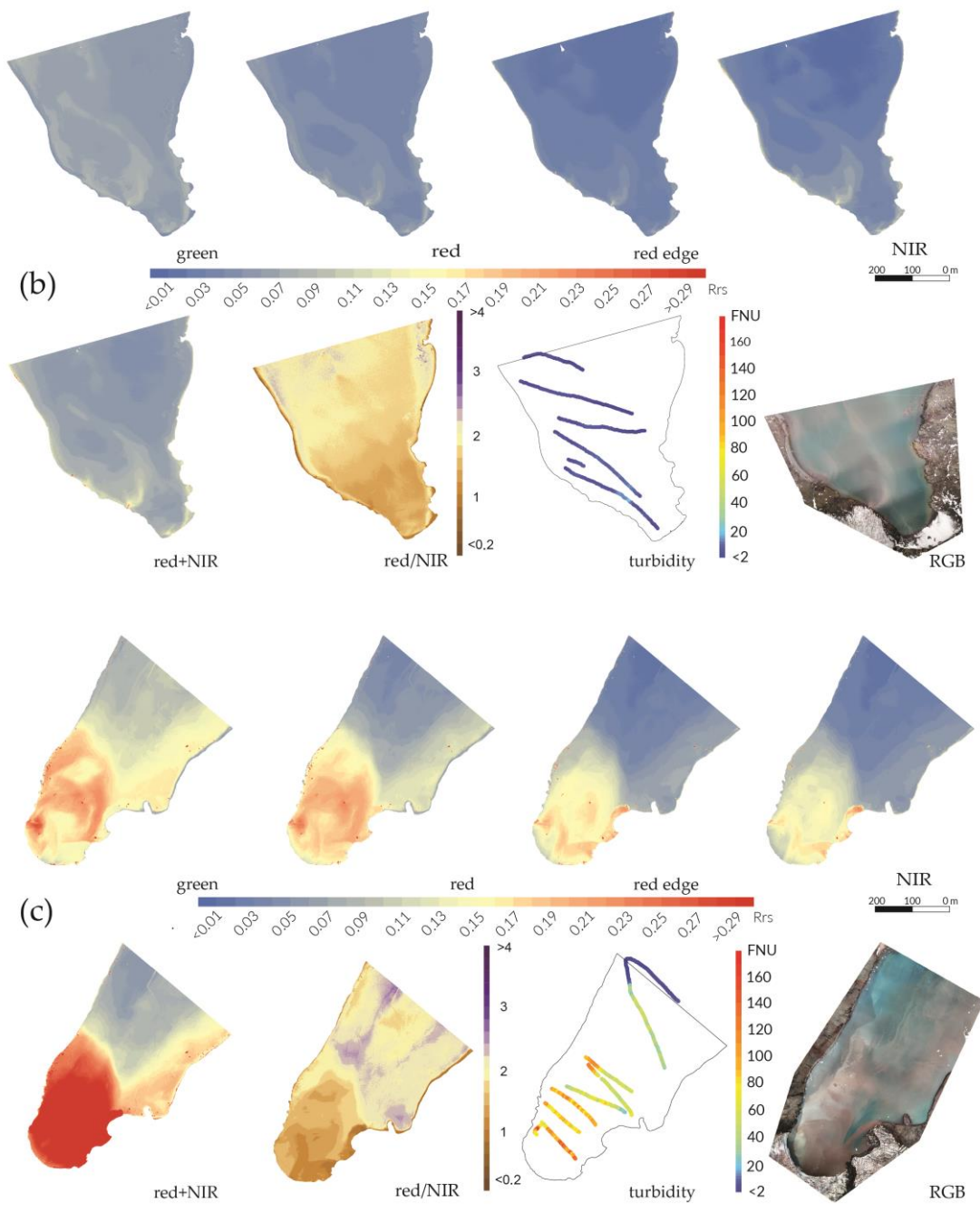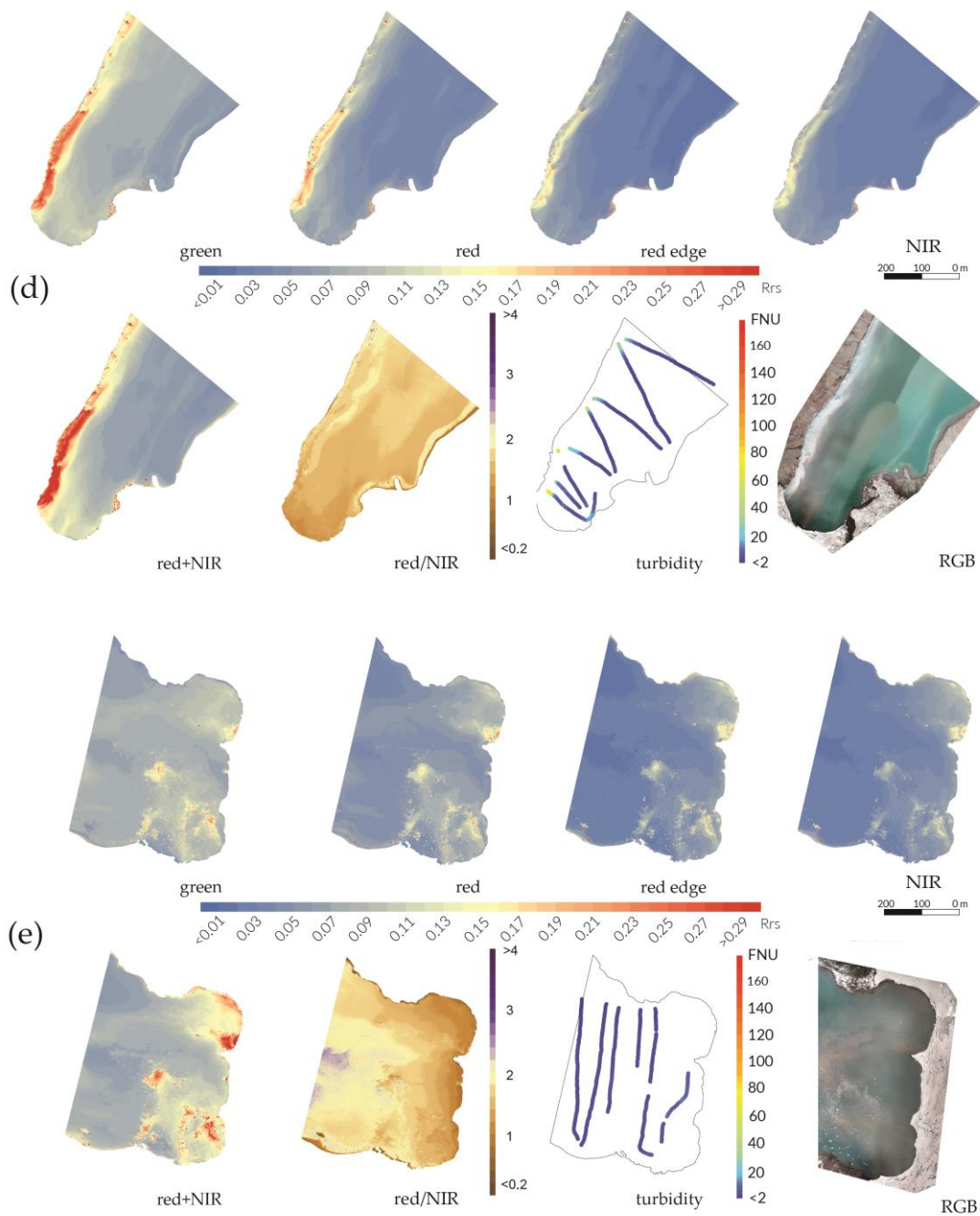

Figure 7. *Cont.*

Figure 7. *Cont.*

Figure 7. Reflectance maps, orthophotomaps, and turbidity maps of the selected glacier bays in Admiralty Bay: (**a**) Ecology Glacier, (**b**) Dera Icefall, (**c**) Zalewski Glacier 1, (**d**) Zalewski Glacier 2, and (**e**) Krak Glacier.

Previous works have shown that the turbidity and spectral response can be linear, log-linear, exponential, or logarithmic. Lower SSCs cause a linear increase in the turbidity. If the amount of particle matter increases, a non-linear increase in the turbidity is observed [53]. The sensitivity of a single band is decreased with increasing turbidity and becomes less linear [32].

Due to moderate FNU values measured in the research areas, a linear relationship and correlation between the registered *in situ* turbidity and the mean reflectance values of each band from the 1-m-radius buffer area was used (Figure 8, Table 4). A good relationship was found between the turbidity and reflectance in the red ($r^2 > 0.45$), RE ($r^2 > 0.5$), and NIR ($r^2 > 0.5$) spectral bands within coves without mélange and where the turbidity oscillated by 100 FNU (Figure 8b–d, Table 4). The colour of the sediment also had an impact on the relation between the light reflectance and water turbidity, and the highest r^2 (>0.7) was noted in areas of subglacial discharges with uniform colouring (Figure 8d). A distinct event was observed near Zalewski Glacier, where two types of sediment were separately discharged. Consequently, the range of the Rrs for equivalent FNU values was mostly dispersed. The lowest r^2 (<0.3) was noted within the coves with ice phenomena, particularly mélange and ice packs. The r^2 value for red+NIR was similar to those noted for single bands. The relationship between the FNU values and the ratio between the red and NIR spectral bands is varied and depends on ice phenomena and sediment type. The r^2 value hovered between 0.004 and 0.420 and is characterized by a high level of uncertainty.

Table 4. Water turbidity and remote sensing reflectance (Rrs) statistics.

| Glacier	Number of Samples	Turbidity Range (FNU)	Spectral Region	Reflectance Range (Rrs)	r^2	*P*-Value	Correlation
Ecology	638	1.91–26.47	530–570 nm	0.02–0.32	0.071	8.85×10^{-12}	0.266
			640–680 nm	0.02–0.38	0.138	2.71×10^{-22}	0.371
			730–740 nm	0.01–0.58	0.064	1.00×10^{-10}	0.252
			770–810 nm	0.01–0.56	0.031	8.05×10^{-6}	0.176
			Red + NIR	0.02–0.80	0.093	3.02×10^{-15}	0.305
			Red/NIR	0.12–20.34	0.020	2.94×10^{-4}	0.143
Dera	353	1.18–23.82	530–570 nm	0.03–0.37	0.339	2.39×10^{-32}	0.582
			640–680 nm	0.02–0.34	0.463	1.13×10^{-47}	0.680
			730–740 nm	0.01–0.40	0.504	1.53×10^{-53}	0.710
			770–810 nm	0.01–0.34	0.501	4.27×10^{-53}	0.708
			Red + NIR	0.04–0.67	0.506	8.10×10^{-54}	0.711
			Red/NIR	0.11–3.33	0.294	1.90×10^{-27}	−0.542
Zalewski 1	445	1.74–167.35	530–570 nm	0.05–0.86	0.358	2.19×10^{-38}	0.598
			640–680 nm	0.03–0.75	0.476	4.10×10^{-55}	0.690
			730–740 nm	0.01–0.83	0.497	1.77×10^{-58}	0.705
			770–810 nm	0.01–0.68	0.498	1.01×10^{-58}	0.706
			Red + NIR	0.05–1.41	0.496	2.07×10^{-58}	0.705
			Red/NIR	0.29–3.44	0.420	9.26×10^{-47}	−0.648
Zalewski 2	451	1.18–97.65	530–570 nm	0.03–0.62	0.727	6.39×10^{-129}	0.853
			640–680 nm	0.03–0.57	0.718	6.82×10^{-126}	0.848
			730–740 nm	0.01–0.63	0.702	2.59×10^{-120}	0.838
			770–810 nm	0.02–0.55	0.685	7.44×10^{-115}	0.827
			Red + NIR	0.04–1.06	0.715	7.46×10^{-125}	0.846
			Red/NIR	0.27–6.53	0.004	1.81×10^{-1}	−0.063
Krak	626	1.19–11.39	530–570 nm	0.03–0.70	0.100	5.66×10^{-16}	0.316
			640–680 nm	0.02–0.92	0.166	1.67×10^{-26}	0.408
			730–740 nm	0.01–1.09	0.256	5.90×10^{-42}	0.506
			770–810 nm	0.01–1.10	0.270	1.47×10^{-44}	0.519
			Red + NIR	0.05–2.02	0.219	2.66×10^{-35}	0.467
			Red/NIR	0.13–12.53	0.159	2.61×10^{-25}	−0.399
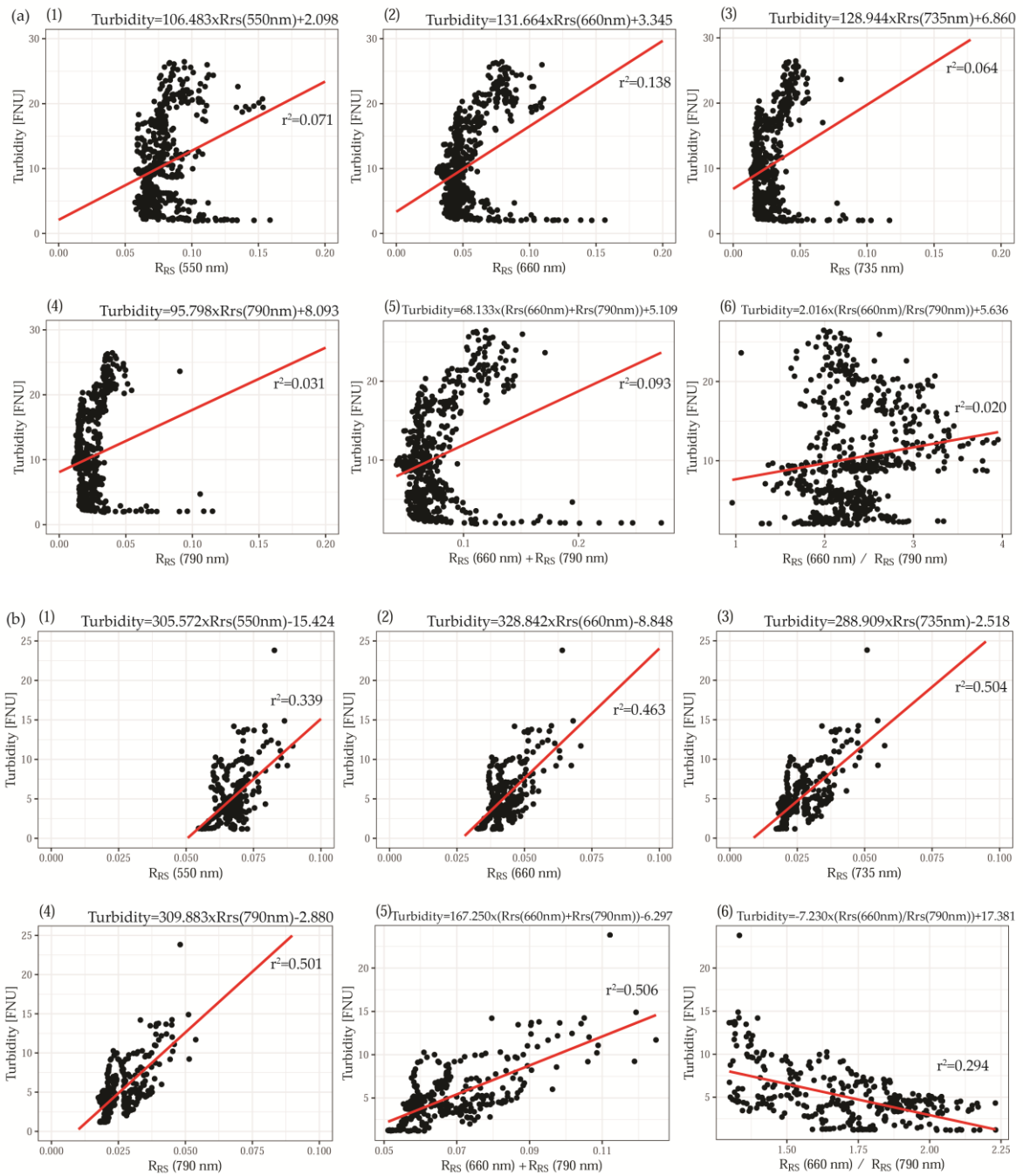
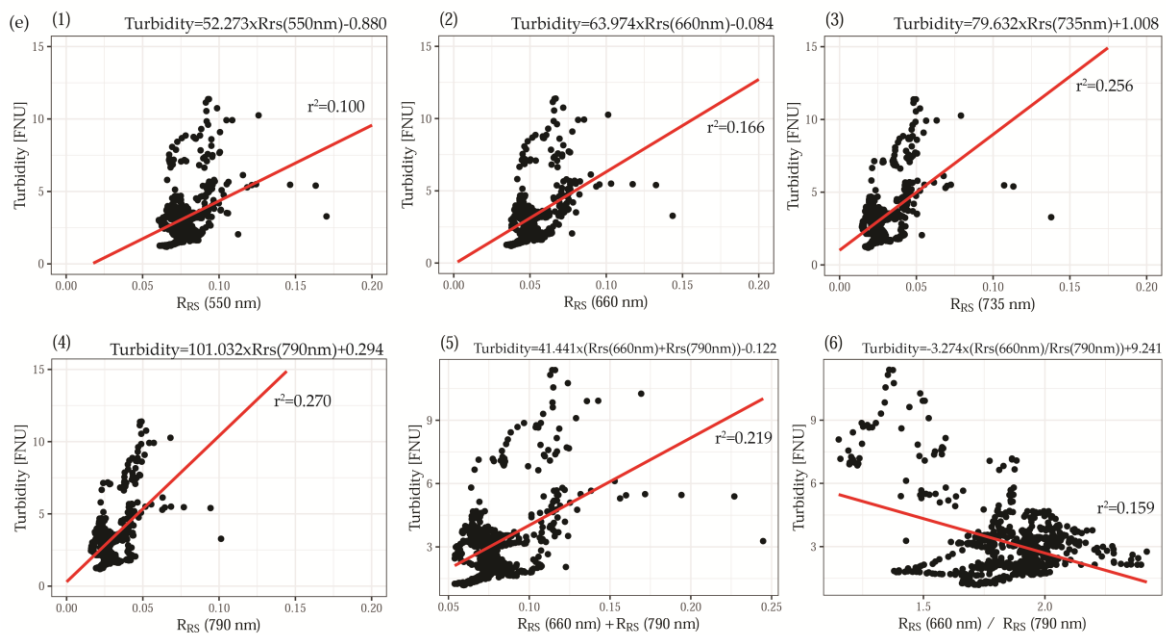**Figure 8.** *Cont.*
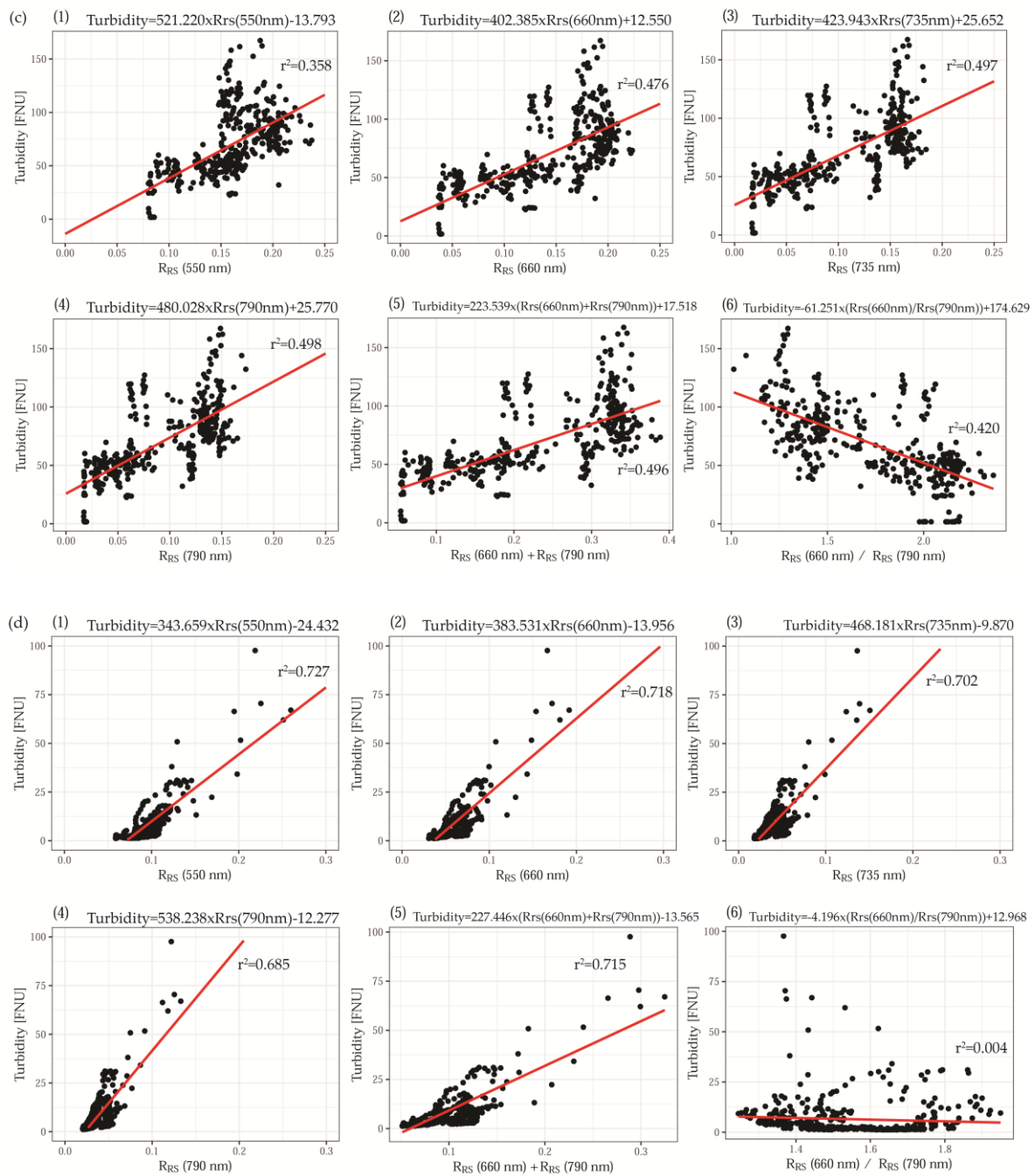
Figure 8. *Cont.*

Figure 8. Scatter plots of the turbidity (FNU) versus the Rrs (550 nm, 660 nm, 735 nm, and 790 nm) for measurements performed on selected glaciers: (**a**) Ecology Glacier, (**b**) Dera Icefall, (**c**) Zalewski Glacier 1, (**d**) Zalewski Glacier 2, and (**e**) Krak Glacier.

4. Discussion

Our research showed the usefulness of multispectral imagery using a UAV for mapping turbidity plumes in Antarctica. With the use of Parrot Bluegrass, images (14 cm) with a pixel range that is 70 times higher than that of Sentinel-2 satellite imagery (10 m) were obtained, which allowed observations of microscale phenomena. Gathering similar resolution imagery from commercial sensors (e.g., WorldView and Pleiades) may generate considerable costs and would be unprofitable. The utilization of drones allowed a more flexible measurement schedule, which is an advantage over satellite information, which is acquired at fixed intervals. An additional benefit of using UAV is its flight altitude, which is low enough to largely eliminate atmospheric impacts. This benefit is especially important with multispectral sensors, for which 90%–99% of cases register signals from atmospheric molecules and aerosols, which requires atmospheric correction tools in satellite imagery [54].

In the present work, the focus on identifying glacial outflows establishes the best reflectance band to retrieve shapes and types (colours) of sediment plumes and fit the best linear relationship between the turbidity and reflectance. Using high-frequency images produced by a Zenmuse X5 camera identified glacial discharges with sediment colour distinction, and images from the Parrot Sequoia+ sensor produced data on the reflectance of turbid waters.

Due to the use of the maximum RGB algorithm, two types of sediment were distinguished in the RGB images. Sediment A has a predominance of red, and sediment B contains green and blue. Through overlapping multispectral images with the RGB photograph and comparing the shapes of different plumes, it was shown that the reflectance range of particular wavelength bands for sediment A and sediment B differ. The analysis of the shapes of plumes allowed us to state that the red band correlates best with low-turbidity and medium-turbidity waters (<70 FNU) [48], which is in accordance with previous research carried out in other parts of the world [32,36,55,56]. However, when the water turbidity exceeds 70 FNU, it correlates most strongly with longer wavelengths, as was noticed by Yafei [57]. Unfortunately, in instances of cove waters covered with ice, an analysis is not possible due to immense light reflection, especially in the green spectral band, which makes green wavelengths poor indicators for spectral analyses of water turbidity levels in polar regions. Based on the two most reliable spectra, two band formulas have been tested. Red+NIR and red/NIR maps have been created,

which have the advantage of reducing noise influencing multispectral images of water [58]. They also reduce the influence of the atmosphere and sun glints on the water surface [59,60]. Overlapping the images of both combinations allows the identification of low-turbidity and medium-turbidity areas and eliminates the influence of ice packs and mélange.

The best linear relationship ($r^2 > 0.7$) between the turbidity and reflectance was found in the case of no ice phenomena on the water surface with homogeneous sediment-rich plumes and in high turbid waters (<70 FNU). The highest correlation coefficient values (>0.8) between the water turbidity and the Rrs were noted for the red, RE, and NIR wavelengths. The simultaneous occurrence of two types of sediment and lower turbidity caused an attenuation of the correlation between the two variables. Due to ice phenomena on the water surface, linear regression is inappropriate. These results are similar to data from previous research in the Arctic, where red light reflectance provided by satellite imagery was affected by the water turbidity values. From these studies, the determination coefficients were $r^2 = 0.70$ for Landsat 8 [61] and $r^2 = 0.90$ [62] and $r^2 = 0.89$ [13] for the Moderate Resolution Imaging Spectroradiometer (MODIS).

It should be noted, however, that this method has its limitations. First, it is applicable for only small bodies of water. The georeferencing of particular images cannot be performed for uniform water areas if each photograph does not involve software to combine consecutive shots [58], which can lead to artefacts and generate errors in the X,Y surface (Table 3). Multispectral images of shallow water areas can also be affected by additional reflectance from the water bottom, which may strengthen the signal [54], especially in shorter wavelengths (i.e., the green spectral band). The identification of glacial discharge can be affected through a number of phenomena: ice packs affect the imagery and release sediment particles into the water during melting and glacial calving, which, in cases of shallow fjords, can cause resuspension sediment particles from the sea floor [63]. Errors can also be introduced through water movement and plume rearrangement within the time between the flyover and the *in situ* measurements. Errors can also be produced by data aggregation, both in the overlapping of images from Parrot Sequoia+ (14-cm pixel resolution) and Zenmuse X5 (2-cm pixel resolution) and in joining the *in situ* measurement data.

The analysis of turbidity or similar measures for the identification of glacial discharges was previously described in studies in both the Arctic and Antarctic regions [19,64,65]. However, combining it with remote sensing methods is less common in the Antarctic [66]. There has been no previous work concerning the utilization of drones with multispectral cameras for monitoring glacial sediment plumes. The Parrot Sequoia+ multispectral camera is mainly used in precision agriculture, and there are very few publications concerning its utilization for hydrological investigations. Previous studies referred to, among others, SSCs in different water layers in rivers [58], the precision of digital surface models (DSM) in water pools based on multispectral camera pictures [67], or assessments of the ecological integrity of wetlands through multispectral mapping [68]. Nonetheless, there are no findings confirming the applicability of using multispectral UAVs for research on polar marine areas. This innovative study suggests the vast potential for using multispectral drone-borne sensors in analysing water surfaces, even in the hostile topographic and meteorological conditions that are found in the lagoons and coves of tidewater glacier termini. This study presents the possibility of using drones in places in which traditional remote sensing methods are not applicable. These places include areas with high cloud coverage such as the Southern Shetlands [69,70] and where microscale processes such as the transport of sediment by runoff and sediment plume dispersion affect the water bodies. This study can be groundwork for further research into marine and lake environments in polar regions, which, in times of climate change, are the subject of intensive transformation [71].

5. Conclusions

In this study, the utilization of the Parrot Sequoia+ multispectral sensor installed on the Parrot Bluegrass UAV was tested. The results provide support for the use of multispectral sensors given by the Zenmuse X5 camera on an Inspire 2 quadcopter drone, which, due to its high-resolution photographs

in the natural RGB colour model, identified glacial discharges as well as the recognition of plume shapes and colours.

The research shows that the Parrot Sequoia+ camera can be successfully used for the analysis of water turbidity. Red wavelengths are applicable for identifying values representing low-turbidity and medium-turbidity waters (<70 FNU) and for identifying red (sediment A) and white sediments (sediment B) in water. In cases of high turbidity in water surface layers, the use of longer wavelengths, such as RE and NIR wavelengths, is suggested. UAV technology allowed the observation of ice phenomena (i.e., mélanges, growlers, ice packs) that prevent this type of analysis or interfere with its results. Sediment type also has an impact since it causes disparities in the electromagnetic reflectance values in different spectral ranges. The UAV methodology is more applicable for small-scale observations, such as those described here, than traditional remote sensing techniques. Using low-resolution satellite imagery from MODIS and Landsat 8 does not register such phenomena and generates a high level of uncertainty.

The Parrot Bluegrass and Inspire 2 UAVs can be effectively used in the Antarctic, even in unfavourable meteorological conditions such as low air temperatures. However, the wind speed oscillated by 5 ms^{-1}, and no precipitation was observed. This study presents new opportunities for using multispectral remote sensing with UAVs in such fields as oceanography and geology, which gives an innovative outlook on research in areas that are difficult to reach by both remote and *in situ* methods.

References

1. Intergovernmental Panel on Climate Change (IPCC). The latest comprehensive assessment of the state and future of the climate system, based on observations and Earth system models. In *Climate Change 2013: The Physical Science Basis. Contribution of Working GroupItothe Fifth Assessment Report of the Intergovernmental Panel on Climate Change*; Stocker, T.F., Qin, D., Plattner, G.-K., Tignor, M., Allen, S.K., Boschung, J., Nauels, A., Xia, Y., Bex, V., Midgley, P.M., Eds.; Cambridge University Press: Cambridge, UK, 2013.
2. Rintoul, S.R.; Chown, S.L.; DeConto, R.M.; England, M.H.; Fricker, H.A.; Masson-Delmotte, V.; Naish, T.R.; Siegert, M.J.; Xavier, J.C. Choosing the future of Antarctica. *Nature* **2018**, *558*, 233–241. [CrossRef] [PubMed]
3. Turner, J.; Colwell, S.R.; Marshall, G.J.; Lachlan-Cope, T.A. Antarctic climate change during the last 50 years. *Int. J. Climatol.* **2005**, *25*, 279–294. [CrossRef]
4. Rückamp, M.; Braun, M.; Suckro, S.; Blindow, N. Observed glacial changes on the King George Island ice cap, Antarctica in the last decade. *Glob. Planet. Chang.* **2011**, *79*, 99–109. [CrossRef]
5. Oliva, M.; Navarro, F.; Hrbáček, F.; Hernández, A.; Nývlt, D.; Pereira, P.; Ruiz-Fernández, J.; Trigo, R. Recent regional climate cooling on the Antarctic Peninsula and associated impacts on the cryosphere. *Sci. Total Environ.* **2017**, *580*, 210–223. [CrossRef] [PubMed]
6. Plenzler, J.; Budzik, T.; Puczko, D.; Bialik, R.J. Climatic conditions at Arctowski Station (King George Island, West Antarctica) in 2013–2017 against the background of regional changes. *Pol. Polar Res.* **2019**, *40*, 1–27.

7. Pritchard, H.D.; Vaughan, D.G. Widespread acceleration of tidewater glaciers on the Antarctic Peninsula. *J. Geophys. Res.* **2007**, *112*, 1–10. [CrossRef]

8. Vaughan, D. Recent trends in melting conditions on the Antarctic Peninsula and their implications for ice-sheet mass balance and sea level. *Arct. Antarct. Alp. Res.* **2006**, *38*, 147–152. [CrossRef]

9. Anderson, R.S.; Anderson, S.P. *Geomorphology: The Mechanics and Chemistry of Landscapes*; Cambridge University Press: Cambridge, UK, 2010.

10. Hudson, B.; Overeem, I.; McGrath, D.; Syvitski, J.P.M.; Mikkelsen, A.; Hasholt, B. MODIS observed increase in duration and spatial extent of sediment plumes in Greenland fjords. *Cryosphere* **2014**, *8*, 1161–1176. [CrossRef]

11. Zajączkowski, M. Sediment supply and fluxes in glacial and outwash fjords, Kongsfjorden and Adventfjorden, Svalbard. *Pol. Polar Res.* **2008**, *29*, 59–72.

12. Sziło, J.; Bialik, R.J. Bedload transport in two creeks at the ice-free area of the Baranowski Glacier, King George Island, West Antarctica. *Pol. Polar Res.* **2017**, *38*, 21–39.

13. Chu, V.W.; Smith, L.C.; Rennermalm, A.K.; Forster, R.R.; Box, J.E. Hydrologic controls on coastal suspended sediment plumes around the Greenland Ice Sheet. *Cryosphere* **2012**, *6*, 1–9. [CrossRef]

14. Motyka, R.J.; Hunter, L.; Echelmeyer, K.A.; Connor, C. Submarine melting at the terminus of a temperate tidewater glacier, LeConte Glacier, Alaska, USA. *Ann. Glac.* **2003**, *36*, 57–65. [CrossRef]

15. Pętlicki, M.; Sziło, J.; MacDonell, S.; Vivero, S.; Bialik, R.J. Recent Deceleration of the Ice Elevation Change of Ecology Glacier (King George Island, Antarctica). *Remote Sens.* **2017**, *9*, 520. [CrossRef]

16. Mugford, R.I.; Dowdeswell, J.A. Modeling glacial meltwater plume dynamics and sedimentation in high-latitude fjords. *J. Geophys. Res.* **2011**, *116*. [CrossRef]

17. Sziło, A.; Bialik, R.J. Grain size distribution of bedload transport in a glaciated catchment (Branowski Glacier, King George Island, Western Antarctica). *Water* **2018**, *10*, 360. [CrossRef]

18. Dowdeswell, J.A.; Hogan, K.A.; Arnold, N.S.; Mugford, R.I.; Wells, M.; Hirst, J.P.P.; Decalf, C. Sediment-rich meltwater plumes and ice-proximal fans at the margins of modern and ancient tidewater glaciers: Observations and modelling. *Sedimentology* **2015**, *62*, 1665–1692. [CrossRef]

19. Meredith, M.P.; Falk, U.; Bers, A.V.; Mackensen, A.; Schloss, I.R.; Ruiz Barlett, E.; Abele, D. Anatomy of a glacial meltwater discharge event in an Antarctic cove. *Philos. Trans. R. Soc. A Math. Phys. Eng. Sci.* **2018**, *376*, 20170163. [CrossRef]

20. Arendt, K.E.; Dutz, J.; Jónasdóttir, S.H.; Jung-Madsen, S.; Mortensen, J.; Møller, E.F.; Nielsen, T.G. Effects of suspended sediments on copepods feeding in a glacial influenced sub-Arctic fjord. *J. Plankton Res.* **2011**, *33*, 1526–1537. [CrossRef]

21. Weslawski, J.M.; Legezynska, J. Glaciers caused zooplankton mortality? *J. Plankton Res.* **1998**, *20*, 1233–1240.

22. Kjelland, M.E.; Woodley, C.M.; Swannack, T.M.; Smith, D.L. A review of the potential effects of suspended sediment on fishes: Potential dredging-related physiological, behavioral, and transgenerational implications. *Environ. Syst. Decis.* **2015**, *35*, 334–350. [CrossRef]

23. Fuentes, V.; Alurralde, G.; Meyer, B.; Aguirre, G.E.; Canepa, A.; Wölfl, A.C.; Schloss, I.R. Glacial melting: An overlooked threat to Antarctic krill. *Sci. Rep.* **2016**, *6*, 27234. [CrossRef] [PubMed]

24. Urbanski, J.A.; Stempniewicz, L.; Węsławski, J.M.; Dragańska-Deja, K.; Wochna, A.; Goc, M.; Iliszko, L. Subglacial discharges create fluctuating foraging hotspots for sea birds in tidewater glacier bays. *Sci. Rep.* **2017**, *7*, 43999. [CrossRef] [PubMed]

25. Maat, D.S.; Prins, M.A.; Brussaard, C.P. Sediments from Arctic Tide-Water Glaciers Remove Coastal Marine Viruses and Delay Host Infection. *Viruses* **2019**, *11*, 123. [CrossRef] [PubMed]

26. Schild, K.M.; Hawley, R.L.; Morriss, B.F. Subglacial hydrology at Rink Isbræ, West Greenland inferred from sediment plume appearance. *Ann. Glaciol.* **2016**, *57*, 118–127. [CrossRef]

27. Bhardway, A.; Joshi, P.K.; Sam, L.; Snehmani. Remote sensing of alpine glaciers in visible and infrared wavelengths: A survey of advances and prospects. *Geocarto Int.* **2015**, *31*, 557–574. [CrossRef]

28. Bhardway, A.; Sam., L.; Martin-Torres, F.J.; Kumar, R. UAVs as remote sensing platform in glaciology: Present applications and future prospects. *Remote Sens. Environ.* **2016**, *175*, 196–204. [CrossRef]

29. Hodgkins, R.; Bryant, R.; Darlington, E.; Brandon, M. Pre-melt-season sediment plume variability at Jökulsárlón, Iceland, a preliminary evaluation using in-situ spectroradiometry and satellite imagery. *Ann. Glaciol.* **2016**, *57*, 39–46. [CrossRef]

30. Dowdeswell, J.A.; Hamilton, G.S.; Hagen, J.O. The duration of the active phase on surge-type glaciers: Contrasts between Svalbard and other regions. *J. Glaciol.* **1991**, *37*, 388–400. [CrossRef]

31. Elverhøi, A.; Lønne, Ø.; Seland, R. Glaciomarine sedimentation in a modern fjord environment, Spitsbergen. *Polar Res.* **1983**, *1*, 127–150. [CrossRef]

32. Dogliotti, A.I.; Ruddick, K.G.; Nechad, B.; Doxaran, D.; Knaeps, E. A single algorithm to retrieve turbidity from remotely-sensed data in all coastal and estuarine waters. *Remote Sens. Environ.* **2015**, *156*, 157–168. [CrossRef]

33. Moore, G.K. Satellite remote sensing of water turbidity. *Hydrol. Sci. Bull.* **1980**, *25*, 407–421. [CrossRef]

34. Garaba, S.P.; Badewien, T.H.; Braun, A.; Schuz, A.C.; Zielinski, O. Using ocean colour remote sensing products to estimate turbidity at the Wadden Sea time series station Spiekeroog. *J. Eur. Opt. Soc. Rapid Publ.* **2014**, *9*. [CrossRef]

35. Odermatt, D.; Gitelson, A.; Brando, V.E.; Schaepman, M. Review of constituent retrieval in optically deep and complex from satellite imagery. *Remote Sens. Environ.* **2012**, *118*, 116–126. [CrossRef]

36. Mouw, C.B.; Greb, S.; Aurin, D.; DiGiacomo, P.M.; Lee, Z.; Twardowski, M.; Binding, C.; Hu, C.; Ma, R.; Moore, T.; et al. Aquatic color radiometry remote sensing of coastal and inland waters: Challenges and recommendations for future satellite missions. *Remote Sens. Environ.* **2015**, *160*, 15–30. [CrossRef]

37. Whitehead, K.; Hugenholtz, C.H. Remote sensing of the environment with small unmanned aircraft systems (UASs), part 1: A review of progress and challenges. *J. Unmanned Veh.* **2014**, *2*, 69–85. [CrossRef]

38. Rymszewicz, A.; O'Sullivan, J.J.; Bruen, M.; Turner, J.N.; Lawler, D.M.; Conroy, E.; Kelly-Quinn, M. Measurement differences between turbidity instruments, and their implications for suspended sediment concentration and load calculations: A sensor inter-comparison study. *J. Environ. Manag.* **2017**, *199*, 90–108. [CrossRef]

39. Pfannkuche, J.; Schmidt, A. Determination of suspended particulate matter concentration from turbidity measurements: Particle size effects and calibration procedures. *Hydrol. Process.* **2003**, *17*, 1951–1963. [CrossRef]

40. Davies-Colley, R.J.; Smith, D.G. Turbidity, suspended sediment and water clarity: A review. *J. Am. Water Res. Assoc.* **2001**, *37*, 1085–1101. [CrossRef]

41. Birkenmajer, K. Admiralty Bay, King George Island (South Shetland Islands, West Antarctica): A geological monograph: In Geological results of the Polish Antarctic expeditions. *Studia Geol. Pol.* **2003**, *120*, 5–73.

42. Majdański, M.; Środa, P.; Malinowski, M.; Czuba, W.; Grad, M.; Guterch, A.; Hegedűs, E. 3D seismic model of the uppermost crust of the Admiralty Bay area, King George Island, West Antarctia. *Pol. Polar Res.* **2008**, *29*, 303–318.

43. Commission on Standardization of Geographical Names outside the Republic of Poland (KSNG). Available online: http://ksng.gugik.gov.pl/english/index.php (accessed on 2 August 2019).

44. Dera, J. Oceanographic investigation on the Ezcurra Inlet during the 2nd Antarctic Expedition of the Polish Academy of Sciences. *Oceanologia* **1980**, *12*, 5–26.

45. Pruszak, Z. Currents circulation in the waters of Admiralty Bay (region of Arctowski Station on King George Island). *Pol. Polar Res.* **1980**, *1*, 55–74.

46. Robakiewicz, M.; Rakusa-Suszczewski, S. Application of 3D circulation model to Admiralty Bay, King George Island, Antarctica. *Pol. Polar Res.* **1999**, *20*, 43–58.

47. Braun, M.H.; Gossman, H. Glacial Changes in the Areas of Admiralty Bay and King George Island, maritime Antarctica. In *Geoecology and Antarctic Ice-Free Coastal Landscapes*; Beyer, L., Bülter, M., Eds.; Springer: Berlin, Germany, 2002; pp. 75–89.

48. EXO User Manual. Available online: https://www.ysi.com/File%20Library/Documents/Manuals/EXO-User-Manual-Web.pdf (accessed on 8 May 2019).

49. Al-amri, S.S.; Kalyankar, N.V.; Khamitkar, S.D. Linear and non-linear contrast enhancement image. *Int. J. Comput. Sci. Netw. Secur.* **2010**, *10*, 139–143.

50. Hussain, M.A.; Akbari, A.S. Max-RGB based colour constancy using the sub-blocks of the image. In Proceedings of the 9th International Conference on Developments in eSystems Engineering (DeSE 2016), 31 August–2 September 2016; pp. 289–294.

51. Van Groenigen, J.W.; Stein, A. Constrained Optimization of Spatial Sampling using Continuous Simulated Annealing. *J. Environ. Qual.* **1998**, *27*, 1078–1086. [CrossRef]

52. Ohashi, Y.; Iida, T.; Sugiyama, S.; Aoki, S. Spatial and temporal variations in high turbidity surface water off the Thule region, northwestern Greenland. *Polar Sci.* **2016**, *10*, 270–277. [CrossRef]

53. Rodrigo, C.; Giglio, S.; Varas, A. Glacier sediment plumes in small bays on the Danco Coast, Antarctic Peninsula. *Antarct. Sci.* **2016**, *28*, 395–404. [CrossRef]

54. Zheng, G.; DiGiacomo, P.M. Uncertainties and applications of satellite-derived coastal water quality products. *Prog. Oceanogr.* **2017**, *159*, 45–72. [CrossRef]

55. Brando, V.E.; Braga, F.; Zaggia, L.; Giardino, C.; Bresciani, M.; Matta, E.; Bellafiore, D.; Ferrarin, C.; Maicu, F.; Benetazzo, A.; et al. High-resolution satellite turbidity and sea surface temperature observations of river plume interactions during a significant flood event. *Ocean Sci.* **2015**, *11*, 909–920. [CrossRef]

56. Quang, N.; Sasaki, J.; Higa, H.; Huan, N.H. Spatiotemporal variation of turbidity based on landsat 8 OLI in CAM Ranh Bay and Thuy Trieu Lagoon, Vietnam. *Water* **2017**, *9*, 570. [CrossRef]

57. Yafei, L.; Doxoran, D.; Ruddick, K.; Shen, F.; Gentili, B.; Yan, L.; Huang, H. Saturation of water reflectance in extremely turbid media based on field measurments, satellite data and bio-optical modelling. *Opt. Express* **2018**, *26*, 10435–10451.

58. Larson, M.D.; SimicMilas, A.; Vincent, R.K.; Evans, J.E. Multi-depth suspended sediment estimation using high-resolution remote-sensing UAV in Maumee River, Ohio. *Int. J. Remote Sens.* **2018**, *39*, 5472–5489. [CrossRef]

59. Doxaran, D.; Froidefond, J.M.; Castaing, P. Remote-sensing reflectance of turbid sediment-dominated waters. Reduction of sediment type variations and changing illumination conditions effects by use of reflectance ratios. *Appl. Opt.* **2003**, *42*, 2623–2634. [CrossRef] [PubMed]

60. Sokoletsky, L.; Fang, S.; Yang, X.; Wei, X. Evaluation of empirical and semianalytical spectral reflectance models for surface suspended sediment concentration in the highly variable estuarine and coastal waters of East China. *IEEE J. Sel. Top. Appl. Earth Obs. Remote Sens.* **2016**, *9*, 5182–5192. [CrossRef]

61. Schild, K.M.; Hawley, R.L.; Chipman, J.W.; Benn, D.I. Quantifying suspended sediment concentration in subglacial sediment plumes discharging from two Svalbard tidewater glaciers using Landsat-8 and in situ measurements. *Int. J. Remote Sens.* **2017**, *38*, 6865–6881. [CrossRef]

62. Chu, V.W.; Smith, L.C.; Rennermalm, A.K.; Forster, R.R.; Box, J.E.; Reeh, N. Sediment plume response to surface melting and supraglacial lake drainages on the Greenland ice sheet. *J. Glaciol.* **2009**, *55*, 1072–1082. [CrossRef]

63. Ashley, G.M.; Smith, N.D. Marine sedimentation at a calving glacier margin. *Geo. Soc. Am. Bull.* **2000**, *112*, 657–668. [CrossRef]

64. Hodgkins, R. Glacier hydrology in Svalbard, Norwegian high arctic. *Quat. Sci. Rev.* **1997**, *16*, 957–973. [CrossRef]

65. Pan, B.J.; Vernet, M.; Reynolds, R.A.; Mitchell, B.G. The optical and biological properties of glacial meltwater in an Antarctic fjord. *PLoS ONE* **2019**, *14*, e0211107. [CrossRef]

66. Sartori, R.Z.; Mendes, J.R.C.W.; Simões, J.C. Análise das mudançasambientais da GeleiraViéville, Baía do Almirantado, IlhaRei George, Antártica. *Pesquisas em Geociências* **2015**, *42*, 61.

67. Vitti, D.M.; Marques Junior, A.; Guimaraes, T.T.; Koste, E.C.; Inocencio, L.C.; Veronez, M.R.; Mauad, F.F. Geometry accuracy of DSM in water body margin obtained from an RGB camera with NIR band and a multispectral sensor embedded in UAV. *Eur. J. Remote Sens.* **2018**, *52*, 160–173. [CrossRef]

68. Diaz-Delgado, R.; Cazacu, C.; Adamescu, M. Rapid Assesment of Ecological Integrity for LTER Wetland Sites by Using UAV Multispectral Mapping. *Drones* **2019**, *3*, 3. [CrossRef]

69. Kejna, M. Topoclimatic conditions in the vicinity of the Arctowski Station (King George Island, Antarctica) during the summer season of 2006/2007. *Pol. Polar Res.* **2008**, *29*, 95–116.

70. Kejna, M.; Laska, K. Weather conditions at Arctowski Station, King George Island, South Shetland Islands, Antarctica in 1996. *Pol. Polar Res.* **1999**, *20*, 203–220.

71. Harley, C.D.; Randall Hughes, A.; Hultgren, K.M.; Miner, B.G.; Sorte, C.J.; Thornber, C.S.; Williams, S.L. The impacts of climate change in coastal marine systems. *Ecol. Lett.* **2006**, *9*, 228–241. [CrossRef]